A&A, 704, A46 (2025)
https://doi.org/10.1051/0004-6361/202555081

Astronomy & Astrophysics

Effect of rotation and metallicity on the explodability of massive stars

Renyu Luo, Chunhua Zhu, Guoliang Lü*, Helei Liu, Sufen Guo*, Lei Li, and Zhuowen Li

School of Physical Science and Technology, Xinjiang University, Urumqi 830046, China

Received 8 April 2025 / Accepted 6 October 2025

ABSTRACT

Context. During the late stages of massive stellar evolution, failed supernovae (FSN) may form through core-collapse processes. The traditional evaluation criterion $\xi_{2.5} = 0.45$, where $\xi_{2.5}$ is the compactness parameter, defined as the mass enclosed within 2.5 $M_\odot$ divided by the radius at that mass in units of 1000 km, is primarily established using nonrotating progenitor models. It is significantly inaccurate when it is applied to rotating pre-supernova systems. The effects of metallicity and rotation on the explodability landscapes of massive stars lack a robust quantification.

Aims. We investigate the effect of rotation and metallicity on the explodability of massive stars.

Methods. Using the code called modules for experiments in stellar astrophysics (MESA), we simulated stars with initial rotational velocities of $V_{\rm ini} = 0$, 300 km s^{-1}, and 600 km s^{-1} at three metallicities ($Z_\odot$, $1/10\,Z_\odot$, and $1/50\,Z_\odot$) and tracked their evolution from the zero-age main sequence (ZAMS) until iron core collapse at 1000 km s^{-1}. For each MESA model at the onset of core collapse, we extracted the key parameters (the enclosed mass, temperature, density, radial velocity, electron fraction, and angular velocity) and input them in the 1D supernova collapse simulation code GR1D to simulate the core-collapse supernova (CCSN) phase. Through an iterative procedure, we determined the critical heating parameter $f_{\rm heat}$ within 1% of the explosion threshold. We then defined the corresponding time-averaged heating efficiency $\bar{\eta}^{\rm crit}_{\rm heat}$ at this $f_{\rm heat}$ to estimate the progenitor explodability. By correlating the explosion outcomes with $\xi_{2.5}$, we derived an explodability criterion based on $\xi_{2.5}$ and also investigated the correlation between explodability and the ZAMS mass and CO-core mass for the rotational velocities and metallicities.

Results. We obtain new critical values of $\xi_{2.5}$ for pre-supernova star explodability under different rotation rates and metallicities: 0.45 for models with $V_{\rm ini} = 0$; 0.48 for the $V_{\rm ini} = 300$ km s^{-1} group; 0.47 for $V_{\rm ini} = 600$ km s^{-1} at $Z = Z_\odot$, and 0.59 for low metallicity ($Z = 1/10$ and $1/50\,Z_\odot$). These criteria enable the rapid assessment of the progenitor explodability for equation of state configurations resembling LS220, which is an equation of state with a nuclear incompressibility of 220 MeV. The upper limit of the pre-supernova star compactness for producing CCSNe is significantly higher in chemically homogeneous evolution (CHE) cases than in non-CHE scenarios. This discrepancy primarily arises because the centrifugal force generated by rotational motion in a pre-supernova star more effectively facilitates explosions than in nonrotating scenarios. According to the explodability criterion of the compactness $\xi_{2.5}$, we give the ZAMS mass ranges for FSN in different models. We also determined the position of the CO-core mass corresponding to the compactness peak. Our results show that CHE undergone by rapidly rotating low-metallicity massive stars leads to a significant decrease in the ZAMS and CO-core mass range for FSN.

Conclusions. Rotation substantially affects the explodability of low-metallicity massive stars. This underscores that it is important to incorporate rotational effects in models of CCSN progenitors.

Key words. neutrinos – shock waves – stars: evolution – stars: massive – stars: rotation – supernovae: general

1. Introduction

At the conclusion of massive star evolution, when the electron degeneracy pressure is no longer sufficient to counteract gravitational forces, the iron core undergoes collapse. Upon reaching nuclear saturation compactness, neutron degeneracy pressure renders the core rigid and incompressible. The infalling material generates a shock wave as it impacts the core (Janka 2017). The shock wave can weaken and stall as a result of two primary processes: the dissociation of heavy nuclei preceding the shock front (Colgate & White 1966), and the subsequent loss of neutrinos, which leads to the formation of an accretion shock wave (Janka 2017). If the shock wave successfully revives and breaks out of all envelopes, the supernova will successfully explode (Horiuchi et al. 2011; Li et al. 2011), leaving a neutron star, or forming a black hole (BH) via fallback accretion (Kuroda et al. 2018; Chan et al. 2018; Burrows et al. 2023; Heger et al. 2023). If the shock wave revives but fails to break out of the outer envelope, or if the shock wave fails to revive at all, the star will undergo failed supernova (FSN), forming a black hole (Fischer et al. 2009; O'Connor & Ott 2011; Heger et al. 2023; Boccioli et al. 2025). It is very important to understand the mechanics of core-collapse supernovae (CCSNe) and predict which progenitors will undergo explosion (Gogilashvili et al. 2023; Diehl et al. 2021; Fischer et al. 2009; Smartt 2015; Heger et al. 2023).

The prevailing shock-revival theory is the neutrino delayed-heating mechanism proposed by Bethe & Wilson (1985), which has been broadly supported by multidimensional simulations Janka (2025). This theory posits that hundreds of milliseconds after the initial rebound, electron-type neutrinos and antineutrinos transfer thermal energy from the protoneutron star (PNS) to the material located behind the shock wave. When the post-shock material attains sufficient energy, the

* Corresponding authors: guolianglv@xao.ac.cn; 947559540@qq.com

shock wave is revitalized and continues to propagate outward (Janka 2017; Bethe & Wilson 1985). Notably, in the vast majority of one-dimensional (1D) supernova simulations, the neutrino heating mechanism proves inadequate for triggering a supernova explosion (Horowitz 2002; Burrows et al. 2006; Fischer et al. 2017) unless the neutrino heating efficiency is significantly enhanced (Gogilashvili et al. 2023; Liebendörfer et al. 2005; Buras et al. 2006a; Müller et al. 2017; Radice et al. 2017). With the enhancement of computational capabilities, it has become possible to conduct 2D (Miller et al. 1993; Herant et al. 1994) and 3D (Janka & Mueller 1996; Fryer & Warren 2002) CCSNe simulations. Multidimensional simulations can enable successful CCSNe explosions (Lentz et al. 2015; Müller 2015; Bruenn et al. 2016; Müller et al. 2019; Burrows et al. 2020; Vartanyan & Burrows 2023). The advancement of multidimensional simulations has brought to light additional explosion mechanisms, such as neutrino-driven turbulence and convection, which are increasingly recognized for their critical roles in supernova dynamics (Murphy & Burrows 2008; Mabanta & Murphy 2018). Consequently, assessing the potential for a supernova to explode necessitates multidimensional simulations.

Multidimensional simulations are extremely time-consuming and computationally intensive, however (Boccioli et al. 2021; Gogilashvili et al. 2023). In contrast, 1D simulations are significantly faster. O'Connor et al. (2018) conducted a comprehensive comparison of several simulation codes designed to study the CCSNe mechanism and found that the results from most codes were similar. This ensures the reliability of the code and provides a foundation for studying the effects of different parameters on supernova explodability.

Through 1D parametric simulations, certain physical parameters of pre-supernova stars are correlated with their explosive outcomes (Boccioli et al. 2021). These parameters allow us to rapidly assess the potential for pre-supernova stars to explode. To do this, O'Connor & Ott (2011) proposed the compactness parameter $\xi_{2.5}$, Pejcha & Thompson (2015) employed the critical neutrino luminosity, Ertl et al. (2016) also introduced a method using two parameters, and Müller et al. (2016) used five physically motivated parameters to determine the outcomes. More recently, Maltsev et al. (2025) formulated a multiparameter criterion based on a large set of stellar models and achieved an accuracy of >99% in predicting the outcomes of a semi-analytic supernova model.

Of all the models mentioned above, the compactness parameter $\xi_{2.5}$ proposed by O'Connor & Ott (2011) to predict the explodability of pre-supernova stars is the simplest and most widely applied Heger et al. (2023). Some multidimensional simulations have cast doubt on the use of compactness for predicting pre-supernova explodability, however. Examples are the 2D simulations of 100 stars by Vartanyan & Burrows (2023) and Wang et al. (2022), along with the 3D simulations by Burrows et al. (2019, 2020, 2024). The criterion $\xi_{2.5}$ is based on the 1D supernova collapse simulation code GR1D (O'Connor & Ott 2010; O'Connor 2015). Significant difficulties arise in one-dimensional simulations from the absence of neutrino-driven turbulence and convective motion for evaluating explodability. In the simulations, O'Connor & Ott (2011) therefore artificially increased the neutrino heating rate in the post-shock matter until explosions were triggered and then statistically determined the critical time-averaged heating efficiency required ($\eta^{\rm crit}_{\rm heat}$) for a pre-supernova star explosion. They found that a pre-supernova with high compactness ($\xi_{2.5}$) demanded extremely high $\eta^{\rm crit}_{\rm heat}$. Within the neutrino-driven paradigm, these high efficiencies were deemed unlikely, which led to the conclusion that these progenitors would not explode. Ultimately, the authors established a predictive criterion for CCSN explodability based on the pre-supernova star compactness parameter $\xi_{2.5}$. This criterion was primarily established based on nonrotating pre-supernova star models, however. Recent studies (Takiwaki et al. 2016; Summa et al. 2018; Obergaulinger & Aloy 2020; Aguilera-Dena et al. 2020) suggested that centrifugal forces in a rapidly rotating massive pre-supernova star may significantly facilitate neutrino-driven explosions. Consequently, the original compactness-based criterion applied to predict the explodability of rapidly rotating massive pre-supernova stars might lead to erroneous conclusions.

Additionally, the evolution during the main-sequence phase can significantly affect the structure of pre-supernova stars and thereby affect the explosion outcome (Li et al. 2023, 2025). Extensive numerical simulations showed that the final iron core mass of stars does not monotonically increase with initial mass (Timmes et al. 1996; Sukhbold & Woosley 2014; Limongi & Chieffi 2018; Schneider et al. 2021; Temaj et al. 2024; Laplace et al. 2025). Changes in internal mixing, metallicity, and rotation all affect the relation between the initial and final mass of stars (Farrell et al. 2020) and thereby affect the explodability. Rotation can induce various instabilities during the evolutionary process (Heger & Langer 2000) that facilitate chemical mixing and angular momentum transfer Heger et al. (2023). Stellar rotation transports hydrogen from the outer layers to the core-burning region, which accelerates the growth of the helium core and increases its mass. On the other hand, rotational mixing stirs more helium into the envelope, which increases the mean atomic weight of the envelope and reduces its opacity (Sukhbold et al. 2016; Janka et al. 2016; Yoshida et al. 2021). A more massive helium core significantly enhances the stellar luminosity, while the increased helium abundance in the envelope promotes a blue solution (Saio et al. 1988; Langer 1992). Metallicity affects the mass-loss rate, which in turn affects the stellar mass during the evolution. In particular, a low metallicity combined with rapid rotation might lead to a chemically homogeneous evolution (CHE) (Maeder & Meynet 1987; Langer 1992; Brott et al. 2011), which enables the pre-supernova star to retain a higher mass and rotational velocity.

Current multiwavelength observations and theoretical studies collectively indicate that the vast majority of massive stars does not exist in isolation, but rather resides in close binaries or more complex multiple stellar systems (Kobulnicky & Fryer 2007; Sana et al. 2012, 2013, 2014). Massive stars in multiple star systems exchange mass through stable Roche-lobe overflow or merger events during their evolution (Stegmann et al. 2022; Henneco et al. 2024). This implies that the majority of supernovae originates from these mass-exchange objects Moe & Di Stefano (2017), Schneider et al. (2024). From pure helium star models that approximate stripped stars in binaries (Aguilera-Dena et al. 2022, 2023) to binary evolution simulations that incorporate stripped stars, accretors, and mergers (Laplace et al. 2021; Schneider et al. 2021, 2023, 2024), studies collectively demonstrated that binary interactions profoundly shape the pre-collapse core structures of stars. These structural changes directly impact the feasibility of neutrino-driven supernova explosions (Müller et al. 2019; Vartanyan et al. 2021; Woosley et al. 2020; Antoniadis et al. 2022). The complexity of binary and multiple stellar evolution, however, poses unique challenges that extend beyond the scope of this work. We focus on studying the impact of rotation and metallicity on the explodability of massive single stars during their evolution.

We simulated the entire evolution of stars from the main sequence to an explosion to obtain different explodability criteria for $\xi_{2.5}$ in various model groups, and we investigated the effects of rotation and metallicity on the explodability of massive stars. In Section 2 we present the model parameter settings and research methods. In Section 3 we show the results of the study. A brief summary is provided in Section 4.

2. Model

In this section, we present the model parameter settings for the code called modules for experiments in stellar astrophysics (MESA) in version 10398 (Paxton et al. 2011, 2013, 2015, 2018, 2019) and GR1D. We also present the implementation of the (O'Connor & Ott 2011) explosion model and contextualize it against other explosion models.

2.1. Pre-collapse stellar models

We used the open-source 1D stellar evolution simulation code MESA to model the evolution from zero-age main sequence (ZAMS) to core collapse at 1000 km s^{-1}. In the simulations, we configured initial rotational velocities ($V_{\rm ini}$: 0, 300 and 600 km s^{-1}) and metallicities ($Z_\odot$, $1/10\,Z_\odot$, $1/50\,Z_\odot$) with stellar initial masses at ZAMS spanning 10–80 $M_\odot$.

Our MESA parameter settings agree with those of Li et al. (2023), with the exception of the solar metallicity, which we set to 0.014 (Asplund et al. 2009). The mixing-length parameter was $\alpha_{\rm MLT} = 1.5$ (Böhm-Vitense 1958), with hydrogen-burning stage overshooting $\alpha_{\rm ov} = 0.335$ and the semiconvection mixing efficiency $\alpha_{\rm SC} = 0.01$. The rotation can trigger the Goldreich–Schubert–Fricke instability, Eddington–Sweet circulation, dynamical instability, and secular instability, which produce the mixing (Heger et al. 2000). The ratio of turbulent viscosity to the diffusion coefficient was 1/30 (Heger et al. 2000). Stellar winds were modeled according to Yoon et al. (2006), Marchant et al. (2016): For hydrogen-rich stars ($X_{\rm s} > 0.7$), we applied the prescription by Vink et al. (2001); for hydrogen-poor stars ($X_{\rm s} < 0.4$), we adopted the formulas from Hamann et al. (1995); for intermediate compositions ($0.4 \leq X_{\rm s} \leq 0.7$), we employed a linear interpolation. Rotational enhancement of mass loss was included following Bjorkman & Cassinelli (1993). Rotation was limited to $\Omega/\Omega_{\rm crit} < 0.98$ to avoid the critical velocity (Langer 1998; Aguilera-Dena et al. 2020). The models were computed with the MESA `approx21` nuclear network. The parameter `mesh_delta_coeff` was set to 0.5, and `varcontrol_target` was set to 3×10^{-4}.

Following O'Connor & Ott (2011), we still adopted the compactness parameter $\xi_{2.5}$ of pre-supernova stars to quantify their core compactness. The parameter $\xi_{\rm M}$ is defined as

$$\xi_{\rm M} = \frac{M/M_\odot}{R\left(M_{\rm bary} = M\right)/(1000\,{\rm km})}, \tag{1}$$

where M typically represents 2.5 $M_\odot$, and $R(M)$ refers to the radius of a closed region with a baryonic mass of M, which is usually calculated at the core bounce or at a collapse velocity of 1000 km s^{-1}. O'Connor & Ott (2011) provided the criterion for the explodability: when $\xi_{2.5} < 0.45$, a CCSN can successfully explode; otherwise, FSN may occur.

2.2. Core-collapse model

We simulated the CCSNe using GR1D (O'Connor & Ott 2010; O'Connor 2015), an open-source spherically symmetric general-relativistic neutrino-radiation hydrodynamics code. The six input parameters (enclosed mass, temperature, density, radial velocity, electron fraction, and angular velocity) required for each grid point of the progenitor supernova model in GR1D were provided by MESA when the iron core-collapse velocity reached 1000 km s^{-1}. GR1D employs the M1 scheme (O'Connor 2015) for neutrino transport. The M1 transport is a sophisticated neutrino transport method that employs a two-moment scheme to solve the Boltzmann equation governing neutrino propagation (Shibata et al. 2011; Cardall et al. 2013). This transport is more complex than the neutrino transport approach adopted by O'Connor & Ott (2011).

We employed a computational grid comprising 600 radial zones. Within a radius of 20 km, the radial spacing was set to 300 m. Beyond 20 km, the grid extended logarithmically to an outer boundary where the density reaches 2000 g cm^{-3} (higher-resolution simulations are presented in Appendix A). Our simulations included the intrinsic rotation of the progenitor and incorporated an additional parametric neutrino-heating term, whose magnitude was controlled by an adjustable heating coefficient. The equation of state (EOS) we adopted was LS220 (Lattimer & Swesty 1991), featuring a nuclear incompressibility of 220 MeV. Similarly, the neutrino opacity table was generated using NuLib. For LS220, we used the same NuLib table as O'Connor (2015), both using three neutrino flavors and 18 energy groups. The simulations were evolved for a maximum physical time of 2 s. The remaining simulation parameters were set to the recommended values of the GR1D code (broadly consistent with O'Connor 2015). This setting prevented GR1D from terminating prematurely due to constraints in the parameter configuration.

2.3. Neutrino heating

The accretion history of the proto-neutron star (PNS) prior to shock revival determines the outcome: When the PNS accretes enough material to surpass its maximum supported mass (Tolman-Oppenheimer-Volkoff limit), it evolves into a black hole via an FSN; otherwise, a successful CCSN explosion occurs. This approach reflects the fact that in progenitor models where neutrino heating exceeds a critical threshold, sufficient energy deposition can trigger shock revival. To achieve explosion initiation in fully self-consistent 1D spherically symmetric simulations, artificial enhancement of neutrino energy deposition in the post-shock region is typically required. The GR1D code implements neutrino heating through the parameterization of Janka (2001), where the heating rate at radius r is

$$Q^{\rm heat}_{\upsilon_i}(r) = f_{\rm heat}\frac{L_{\upsilon_i}(r)}{4\pi r^2}\sigma_{{\rm heat},\upsilon_i}\frac{\rho}{m_{\rm u}}X_i\left\langle\frac{1}{F_{\upsilon_i}}\right\rangle e^{-2\tau_{\upsilon_i}}, \tag{2}$$

where $f_{\rm heat}$ is a scaling parameter introduced to parametrically amplify the heating rate, $L_{\nu_{\rm i}}(r)$ is the neutrino luminosity interior to a radius r, and i refers to the neutrino flavors. $\tau_{\nu_{\rm i}}$ is the optical depth determined by the leakage scheme. $\sigma_{{\rm heat},\upsilon_i}$ denotes the energy-averaged absorption cross section, and $X_{\rm i}$ is the corresponding mass fraction for the neutrino interactions. The term $\langle 1/F_{\nu_{\rm i}}\rangle$ represents the average inverse flux factor, which is analytically approximated as a function of the optical depth τ by comparison with the angle-dependent radiative transport calculations of Ott et al. (2008).

By increasing the $f_{\rm heat}$ value, we enhanced the neutrino heating, thereby triggering CCSN explosion in 1D simulations. We adopted the same method as O'Connor & Ott (2011) and iteratively adjusted $f_{\rm heat}$ to determine its critical value for explosion, $f_{\rm heat}^{\rm crit}$, within a relative precision of 1%. Figure 1 shows the shock radius evolution with time $t_{\rm bounce}$ for different $f_{\rm heat}$ values. For models with varying $f_{\rm heat}$, the shock emergence times remained identical. At low $f_{\rm heat}$, no explosions occurred in any of the models. As $f_{\rm heat}$ increased, the shock stagnation phase became prolonged. With further increases in $f_{\rm heat}$, the shock propagated outward to the stellar surface and ultimately produced a CCSN. We note that shock waves in both models in the top panel (15 $M_\odot$ ZAMS mass) oscillate with increasing $f_{\rm heat}$ (Buras et al. 2006b), which is absent in the bottom panel (60 $M_\odot$). The top panel requires $f_{\rm heat} \geq 2.58$ (left) and 2.43 (right) for a successful shock revival, and the bottom panel demands $f_{\rm heat} \geq 2.05$ (left) and 2.93 (right), respectively.

While we achieved CCSN explosion in 1D simulations through artificially enhanced neutrino heating in the previous section, it remains unclear whether these models can explode under self-consistent multidimensional natural scenarios with turbulence. Therefore, O'Connor & Ott (2011) used the time-averaged heating efficiency of the critical model ($f_{\rm heat} = f_{\rm heat}^{\rm crit}$), $\bar{\eta}_{\rm heat}^{\rm crit}$. Here, $\bar{\eta}_{\rm heat}$ is defined as (O'Connor & Ott 2011)

$$\bar{\eta}_{\rm heat} = \overline{\int_{\rm gain} \dot{q}_\nu^+ \, dV / (L_{\nu_e} + L_{\bar{\nu}_e})_{r_{\rm gain}}}, \tag{3}$$

where $\dot{q}_\nu^+$ denotes the net energy deposition rate within the gain region, and $(L_{\nu_e} + L_{\bar{\nu}_e})_{r_{\rm gain}}$ represents the luminosity of electron neutrinos and anti-electron neutrinos at the gain radius. We calculated the average value between the shock formation time and the explosion time. The explosion time is defined as the moment when the region behind the shock attains a positive velocity and accretion onto the PNS ceases (in GR1D simulations, outward shock propagation does not necessarily imply outward motion of the material behind the shock; when this point failed to occur, we increased $f_{\rm heat}$ to continue the simulation). $\bar{\eta}_{\rm heat}^{\rm crit}$ characterizes how much of the available neutrino energy must be redeposited on average to explode a given progenitor, regardless of the transport scheme or numerical code (O'Connor & Ott 2011), therefore remains equally valid for the M1 neutrino transport model. By performing 1D simulations of the confirmed eruptive pre-supernova star models, we estimated the required range of $\bar{\eta}_{\rm heat}^{\rm crit}$ values in 1D models that correspond to successful explosions. This approach allowed us to assess via 1D simulations whether a specific progenitor-EOS combination was more likely to result in explosion or BH formation.

Woosley & Weaver (1995) derived $\bar{\eta}_{\rm heat}^{\rm crit} \approx 0.13$ from simulations of a 15 $M_\odot$ ZAMS progenitor with solar metallicity. Buras et al. (2006a) artificially exploded this progenitor in 1D and found $\bar{\eta}_{\rm heat}^{\rm crit}$ ranging from 0.1 to 0.15. O'Connor & Ott (2011) found that their simulated data (EOS was LS180 and LS220) could be clearly divided into two categories: low-compactness models with $\bar{\eta}_{\rm heat}^{\rm crit} \lesssim 0.2$ (the simulations exhibited some noise, with the average value being approximately 0.16, which is close to the value of 0.15 reported by Buras et al. 2006a), and high-compactness models with $\bar{\eta}_{\rm heat}^{\rm crit} \gtrsim 0.23$–$0.27$. Assuming that multidimensional simulations can achieve a fixed heating efficiency regardless of compactness, they proposed that the former category can produce successful explosions while the latter could not. The limitation of this method lies in the fact that this assumption cannot be guaranteed; multidimensional simulations by Boccioli et al. (2025) showed that neutrino heating varies with the compactness. We employed the $\bar{\eta}_{\rm heat}^{\rm crit}$ as the explodability criterion from O'Connor & Ott (2011) and assumed it to be valid for rotating pre-supernova star models.

In Figure 2 we show the temporal evolution of the electron neutrino and antineutrino luminosities $L_{\bar{\nu}_e,\nu_e}$ (solid curves) at the gain radius and the net neutrino energy deposition rate $\dot{q}_\nu^+$ (dashed curves) in the gain layer for the four models in Figure 1 with $f_{\rm heat} = f_{\rm heat}^{\rm crit}$. Using Equation (3), we calculated the critical heating efficiency parameters $\bar{\eta}_{\rm heat}^{\rm crit}$, with the upper panel (left to right) corresponding to 0.112 and 0.139, and the lower panel (left to right) to 0.242 and 0.257. Based on the explodability criterion ($\bar{\eta}_{\rm heat}^{\rm crit} \lesssim 0.2$) in O'Connor & Ott (2011), we determined that the first two models (15 $M_\odot$) would explode, while the latter two (60 $M_\odot$) would form FSN.

For the two pre-supernova star models shown in the lower panels of Figure 1, evolutionary simulations for the critical model cannot be extended further due to limitations in the EOS and neutrino opacity tables. Although shock breakout occurred, they might lead to an FSN if the simulation can be continued, but this continuation cannot always be achieved. We demonstrate that these delayed failed supernova events affect our conclusions very little. First, critical models typically exhibit shock radii approaching or exceeding 1000 km, indicating penetration through most of the stellar envelope. Second, the derived $\bar{\eta}_{\rm heat}^{\rm crit}$ values deviate by only ~3% on average in the numerical resolutions.

2.4. Other explosion models

STIR model. Convection and turbulence are inherently three-dimensional phenomena. The model proposed by Couch et al. (2020) approximates turbulent effects in Newtonian simulations by parameterizing 3D neutrino-driven convection. Boccioli et al. (2021) extended this to a general-relativistic treatment and implemented it in the GR1D+ code. The code is computationally efficient and capable of capturing multi-D neutrino effects. Notably, at the time of writing, the current implementation does not support a simultaneous inclusion of STIR and rotation.

Ertl model. The 1D explosion model of Ertl et al. (2016) and Sukhbold et al. (2016) was based on the prescription by Ugliano et al. (2012). Within their explosion model, the inner 1.1 $M_\odot$ core is removed after bounce and replaced by a moving inner boundary that sets the neutrino energy and luminosity Ugliano et al. (2012). Neutrino transport follows the gray treatment of Scheck et al. (2006). The calibration of the explosion model required the selection of different progenitor models representing SN 1987A and the calibration of the free parameters associated with the core-boundary prescription against the observables of SN 1987A (Ertl et al. 2016; Boccioli et al. 2025). However, Boccioli et al. (2025) identified a key theoretical limitation. The model selects a mild contraction for the 1.1 $M_\odot$ shell, which mildly increases the average neutrino energies over time.

Muller model. The model by Müller et al. (2016) was built upon the theoretical frameworks developed by Janka (2001), Janka (2012), and Müller (2015), among other studies, and expanded upon and refined these frameworks. It does not require complex hydrodynamic simulations, but instead predicts the properties of neutrino-driven explosions based on the pre-collapse stellar structure. The Muller model incorporates the effects of neutrino-driven convection by substituting them with the shock radius multiplied by a scaling factor $\alpha_{\rm turb}$. This causes convection in the explosion model to exert roughly the

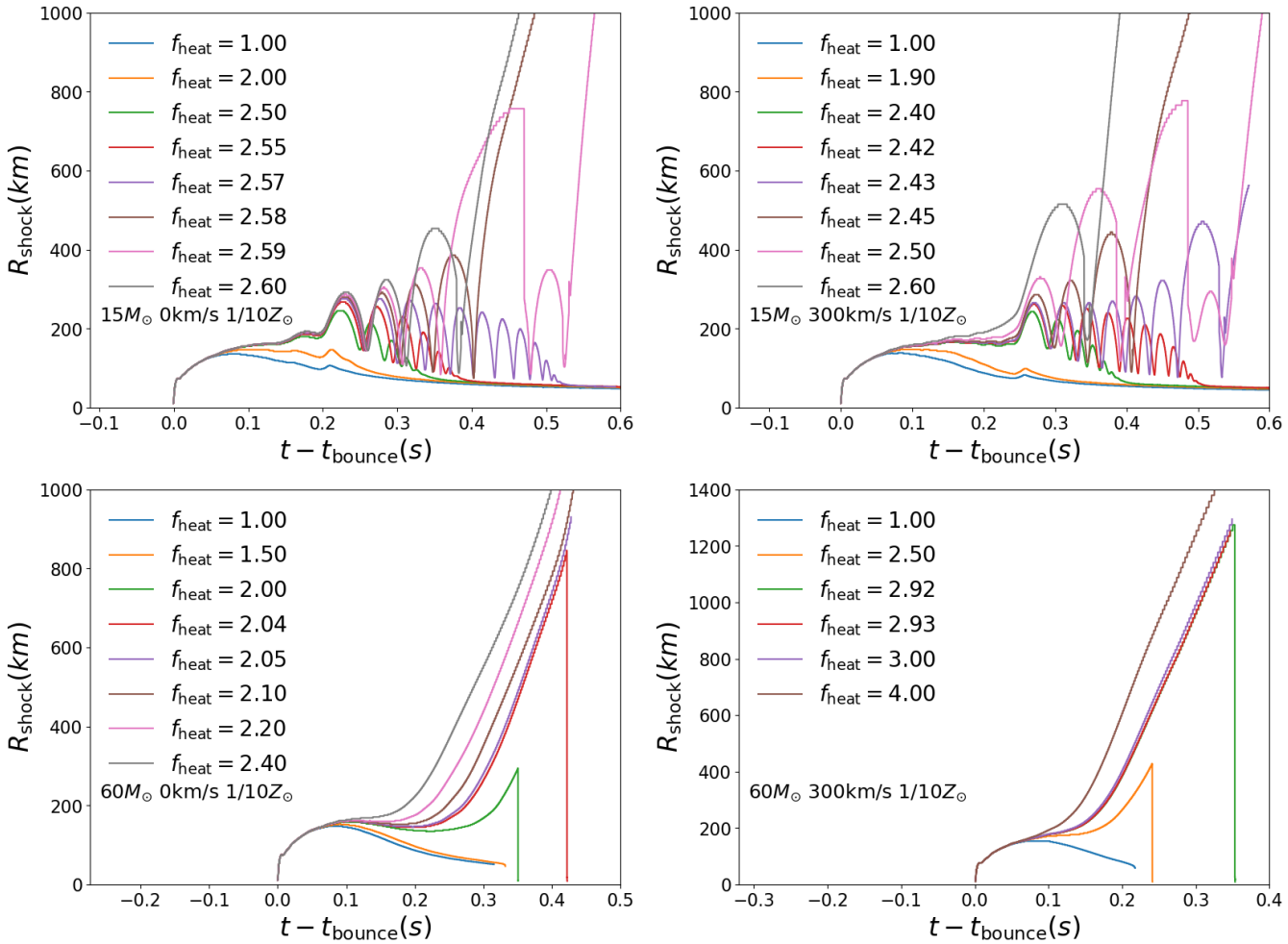

Fig. 1. Shock wave radius evolution vs. explosion time t_{bounce} for different f_{heat} values. The simulations started with an iron core-collapse velocity of 1000 km s^{-1}, where $t = 0$ corresponds to the shock wave formation. The top and bottom panels show 15 $M_\odot$ and 60 $M_\odot$ ZAMS masses, respectively, with initial velocities $V_{ini} = 0$ (left panels) and 300 km s^{-1} (right panels). All models have a metallicity of $1/10\,Z_\odot$.

same influence on all progenitors. Multi-D simulations revealed, however, that the convection strength is strongly correlated with compactness (Boccioli et al. 2025).

These 1D explosion models each have inherent limitations. We chose the explosion model from O'Connor & Ott (2011) because the compactness parameter $\xi_{2.5}$ is a widely adopted and the simplest parameter for predicting the explodability of pre-supernovae star, and GR1D is an open-source software.

3. Results

We computed the critical heating efficiency parameter $\bar{\eta}^{crit}_{heat}$ for each model to assess whether these models can undergo supernova explosions under natural conditions where the nuclear EOS is similar to LS220. The explosion outcomes were then correlated with the compactness parameter $\xi_{2.5}$. Therefore, according to $\bar{\eta}^{crit}_{heat} = 0.2$, we established the explodability criteria of $\xi_{2.5}$ (they can be calculated directly by MESA) for the models with different metallicities and rotational velocities. By analyzing the effect of rapid rotation and metallicity on the explodability of massive stars, we linked their explosion outcomes with their initial ZAMS masses.

3.1. Explodability criteria of $\xi_{2.5}$

Our computational resources were limited, and we therefore only selected a subset of stars from each group for GR1D simulations. We preferentially chose stars with $\xi_{2.5}$ values closest to the threshold.

Figure 3 shows the central angular velocity versus M_{ZAMS} in pre-supernova star models with $V_{ini} = 300$ km s^{-1} (left) and 600 km s^{-1} (right), where different colors indicate distinct metallicities. CHE occurs in all pre-supernova star models with $V_{ini} = 600$ km s^{-1} at both $1/10\,Z_\odot$ and $1/50\,Z_\odot$ metallicities. For the $V_{ini} = 300$ km s^{-1} and $1/50\,Z_\odot$ subset, CHE is exclusively achieved by stars with initial masses $M_{ZAMS} \geq 33\,M_\odot$. These CHE progenitors exhibit systematically higher central angular velocities (ω_{core}), predominantly in the 0.3–0.7 rad s^{-1} range. In contrast, non-CHE progenitors exhibit significantly lower central angular velocities ($\omega_{core} < 0.2$ rad s^{-1}), which may affect the compactness required for the formation of FSN.

Figure 4 shows the $\xi_{2.5}$ values versus their corresponding $\bar{\eta}^{crit}_{heat}$ for all stellar models, with the complete dataset tabulated in Table 1. $\bar{\eta}^{crit}_{heat}$ increases with the augmentation of $\xi_{2.5}$. All our models are clearly divided into two parts by $\bar{\eta}^{crit}_{heat}$: the lower left zone with $\bar{\eta}^{crit}_{heat} \leq 0.2$, and the upper right zone with $\bar{\eta}^{crit}_{heat} \gtrsim 0.23$.

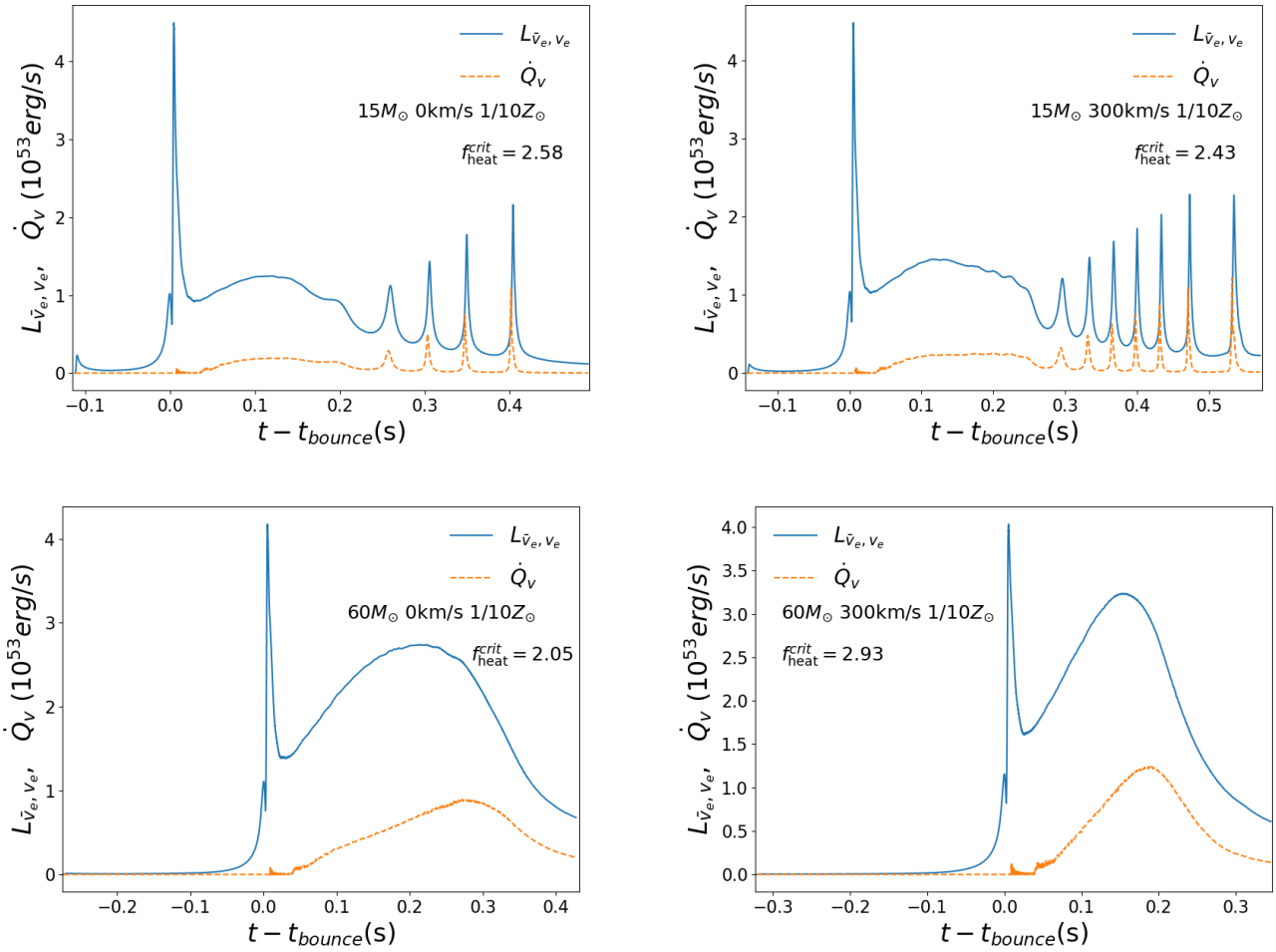

Fig. 2. For $f_{\rm heat} = f_{\rm heat}^{\rm crit}$, we show the evolution of the electron neutrino and antineutrino luminosities $L_{\bar{\nu}_e,\nu_e}$ (solid lines) at the gain radius and the net neutrino energy deposition rate in the gain layer $\dot{Q}_\nu$ ($\int_{\rm gain} \dot{q}_\nu^+ \, dV$, dashed lines) vs. time $t_{\rm bounce}$. The simulations started with an iron core-collapse velocity of 1000 km s^{-1}, where $t = 0$ corresponds to the shock wave formation. The top and bottom panels show 15 $M_\odot$ and 60 $M_\odot$ ZAMS masses, respectively, with initial velocities $V_{\rm ini} = 0$ (left panels) and 300 km s^{-1} (right panels). All models have a metallicity of 1/10 $Z_\odot$.

Based on the explodability criterion of O'Connor & Ott (2011), the former would successfully undergo CCSN, while the latter would evolve into FSN.

The left panel represents models with a ZAMS rotation of zero. The hollow inverted triangular data points are from O'Connor & Ott (2011), which include both LS180 and LS220 EOS with metallicities of $Z_\odot$ and $10^{-4}\,Z_\odot$. A unified criterion of $\xi_{2.5} = 0.45$ is established for all nonrotating models across three metallicities in our work, consistent with the results of O'Connor & Ott (2011). The two models (lower right corner in the left panel) from O'Connor & Ott (2011) exhibit high compactness ($\xi_{2.5} > 0.45$), but still explode with $\bar{\eta}_{\rm heat}^{\rm crit} < 0.2$ because these models feature compositional interfaces where the density drops by 50%; when the shock reaches this interface, it rapidly breaks out, leading to a CCSN explosion (O'Connor & Ott 2011).

For the middle panel with $V_{\rm ini} = 300$ km s^{-1}, the majority of pre-supernova star did not undergo CHE, retaining low rotation rates ($\omega_c \leq 0.2$; Fig. 3 (left panel)). Stars with 1/50 $Z_\odot$ and $M_{\rm ZAMS} \geq 33\,M_\odot$ undergo CHE, but none of our selected models exploded because of their exceptionally high compactness. We still attempted to construct a unified explodability criterion for the metallicities and derived $\xi_{2.5} = 0.48$.

In the right panel, with $V_{\rm ini} = 600$ km s^{-1}, $Z_\odot$ models exhibit lower pre-supernova star rotational velocities because their mass-loss rates are higher (Fig. 3 (right panel)), while the 1/10 $Z_\odot$ and 1/50 $Z_\odot$ models maintain higher rotation before collapse as a result of CHE. The $\xi_{2.5}$ ranges for CCSN explosions between these two groups are significantly different. No unified criterion can be established: We obtained $\xi_{2.5} = 0.47$ for non-CHE models and $\xi_{2.5} = 0.59$ for CHE models. Using the pre-supernova star models simulated by Aguilera-Dena et al. (2020) ($V_{\rm ini} = 600$ km s^{-1}, Z = 1/50 $Z_\odot$), Halevi et al. (2023) calculated the compactness parameter $\xi_{2.5}$ for rapidly rotating massive stars, and they derived $\xi_{2.5} \sim 0.6$ for the explodability criterion, which is consistent with our results. The 12 $M_\odot$ star with 1/10 $Z_\odot$ cannot successfully explode although $\xi_{2.5} < 0.59$ as $\bar{\eta}_{\rm heat}^{\rm crit} > 0.22$. This is primarily due to the low central rotation speed of its progenitor (weak centrifugal support) combined with excessive compactness.

For different model groups, we obtained distinct critical compactness criteria for explodability. By comparing them with the angular velocity $\omega_{\rm c}$ at the pre-supernova star center in Figure 3, we attribute this difference primarily to rotation. Higher pre-supernova star rotational velocities generate stronger centrifugal forces, which facilitate the explosion

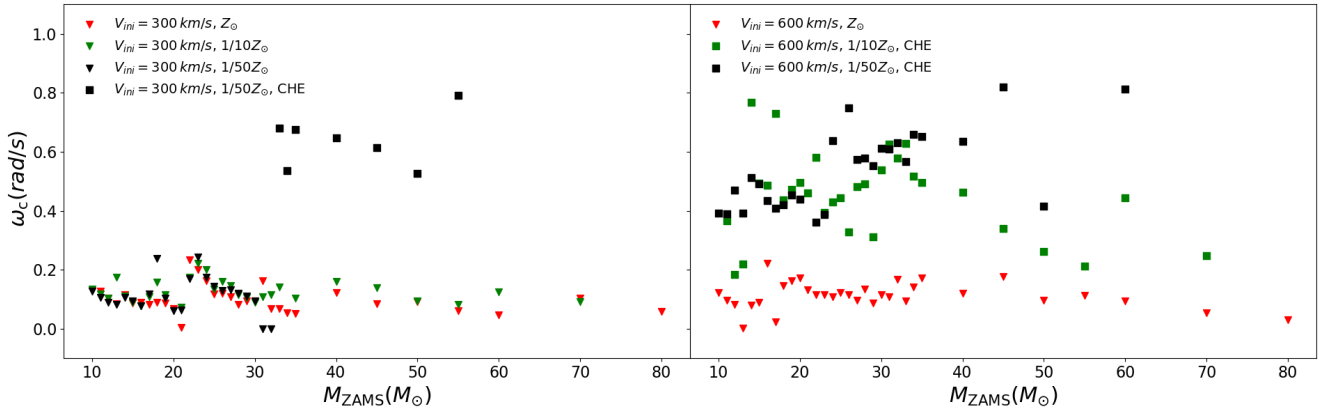

Fig. 3. Central angular velocity (ω_c) at a pre-supernova star for different ZAMS mass models vs. various $V_{\rm ini}$ and metallicities. The left and right panels represent $V_{\rm ini} = 300\,{\rm km\,s^{-1}}$ and $V_{\rm ini} = 600\,{\rm km\,s^{-1}}$, respectively. Metallicities of $Z_\odot$, $1/10\,Z_\odot$, and $1/50\,Z_\odot$, are shown in red, green, and black, respectively. The squares mark the occurrence of CHE.

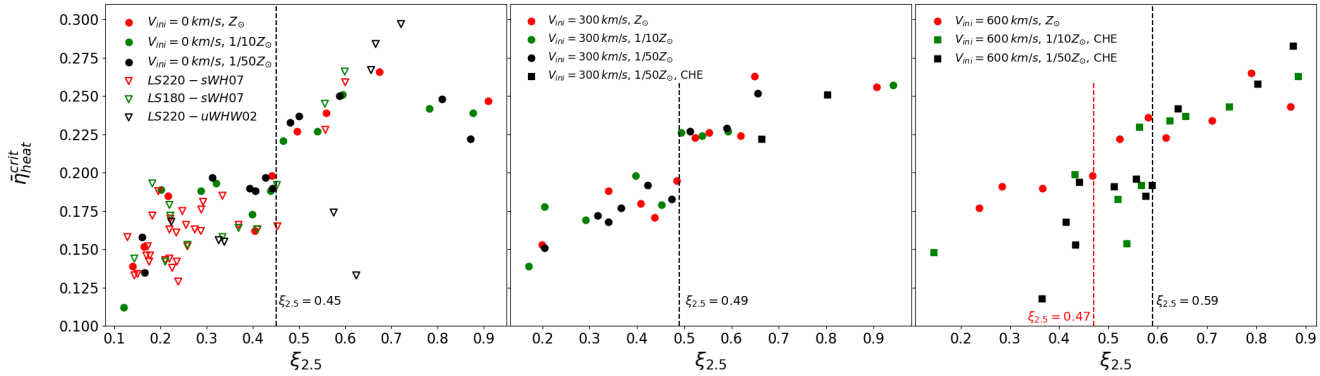

Fig. 4. Compactness parameter $\xi_{2.5}$ vs. the critical model time-averaged heating efficiency $\bar{\eta}^{\rm crit}_{\rm heat}$. The left, center, and right panels correspond to initial velocities $V_{\rm ini} = 0$, $300\,{\rm km\,s^{-1}}$, and $600\,{\rm km\,s^{-1}}$, respectively. The data points in red, green, and black denote metallicities $Z_\odot$, $1/10\,Z_\odot$, and $1/50\,Z_\odot$. The squares mark the occurrence of CHE. The hollow inverted triangles were calculated by O'Connor & Ott (2011), and the combinations of EOS and models LS220-sWH07, LS180-sWH07, and LS220-uWHW02 are represented in red, green, and black, respectively.

(Takiwaki et al. 2016; Summa et al. 2018; Aguilera-Dena et al. 2020; Obergaulinger & Aloy 2020) and thereby increase the upper limit of the critical compactness required for explosion.

Single parameters cannot always reliably predict the progenitor explosibility. Furthermore, the evolution of stars on the main sequence is inherently complex: Even for ZAMS stars with identical rotation and metallicity, the density profiles and rotational properties of their pre-supernova stars can be significantly different. These factors collectively mean that it is challenging to establish a unified explodability criterion for model groups with identical ZAMS conditions but varying masses. Our results reflect an overarching trend for all parameters.

3.2. Explodability of massive stars based on the ZAMS and CO-core masses

As discussed in Section 3.1, the explodability of massive stars is determined by their metallicity, rotation, and specific ZAMS masses. In this section, we present the relation between explodability criteria and ZAMS masses in our models.

Figure 5 shows the pre-supernova star compactness parameter $\xi_{2.5}$ versus initial mass. Our results exhibit a trend similar to that of Li et al. (2023) and Aguilera-Dena et al. (2020). The $\xi_{2.5}$ of our current model shows no significant positive correlation with M_{ZAMS}, which is consistent with the simulated results reported in other studies (Timmes et al. 1996; Schneider et al. 2021; Temaj et al. 2024). The final compactness, central entropy, iron-core mass, and binding energy as functions of initial mass follow similar patterns (Sukhbold & Woosley 2014; Takahashi et al. 2023; Schneider et al. 2021, 2024; Temaj et al. 2024). Laplace et al. (2025) investigated the underlying cause of this distinctive distribution. Taking the left panel of Fig. 5 as an example, Laplace et al. (2025) attributed the increasing compactness at ∼10–20 $M_\odot$ and ∼25–30 $M_\odot$ to the following reason: When the neutrino energy loss exceeds the energy released by carbon/neon burning, the core contracts, driving the burning front outward. As the M_{ZAMS} increases, a larger carbon/neon-free core forms at the center, ultimately yielding a more massive and denser iron core with higher compactness. In contrast, the compactness of stars with masses of ∼20–25 $M_\odot$ and ∼30–35 $M_\odot$ decreases. Laplace et al. (2025) argued that this drop is due to the earlier ignition of subsequent burning episodes, which slows down the progression of the carbon and oxygen burning fronts, caused by two factors: (1) the shortening of the main burning phase caused by fuel depletion and rising temperatures, and (2) the acceleration of core contraction when the fuel-depleted core exceeds the effective Chandrasekhar mass, leading to destabilization of electron degeneracy and accelerated collapse. These

Table 1. Summary of the core-collapse simulation parameters and explosion outcomes for all stellar models.

M ($M_\odot$)	$\xi_{2.5}$	$M_{\rm bary}$ ($M_\odot$)	$M_{\rm grav}$ ($M_\odot$)	$t_{\rm bounce}$ (s)	$t_{\rm f}$ (s)	$f_{\rm heat}^{\rm crit}$	$\bar{\eta}_{\rm heat}^{\rm crit}$	*Explosion*
$V_{\rm ini} = 0\,{\rm km\,s^{-1}}$ $Z_\odot$								
14	0.164	1.82	1.75	0.145	0.723	2.47	0.152	yes
15	0.216	1.93	1.84	0.216	0.662	2.28	0.185	yes
19	0.441	2.26	2.13	0.232	0.733	1.98	0.198	yes
25	0.140	1.70	1.64	0.109	0.634	2.64	0.139	yes
30	0.495	2.35	2.20	0.217	0.877	1.94	0.227	no
33	0.675	2.38	2.25	0.256	0.846	1.93	0.266	no
45	0.404	2.06	1.96	0.182	0.623	2.13	0.162	yes
55	0.558	2.37	2.23	0.250	0.945	1.93	0.239	no
80	0.910	2.25	2.17	0.345	0.562	4.75	0.247	no
$V_{\rm ini} = 0\,{\rm km\,s^{-1}}$ $1/10\,Z_\odot$								
14	0.201	1.91	1.83	0.149	0.753	2.29	0.189	yes
15	0.120	1.91	1.83	0.106	0.620	2.58	0.112	yes
17	0.287	2.02	1.93	0.184	0.787	2.20	0.188	yes
21	0.466	2.30	2.16	0.196	0.794	1.96	0.221	no
23	0.438	2.23	2.10	0.171	0.787	1.98	0.188	yes
29	0.321	2.18	2.06	0.150	0.655	2.03	0.193	yes
32	0.539	2.33	2.19	0.217	0.754	1.92	0.227	no
35	0.594	2.34	2.21	0.250	0.863	1.90	0.251	no
45	0.398	2.04	1.95	0.205	0.675	2.21	0.173	yes
60	0.782	2.41	2.30	0.273	0.701	2.05	0.242	no
80	0.877	2.31	2.22	0.266	0.513	3.59	0.239	no
$V_{\rm ini} = 0\,{\rm km\,s^{-1}}$ $1/50\,Z_\odot$								
13	0.159	1.82	1.75	0.094	0.600	2.45	0.158	yes
15	0.165	1.79	1.72	0.165	0.690	2.50	0.135	yes
17	0.312	2.17	2.04	0.161	0.728	2.08	0.197	yes
23	0.442	2.24	2.12	0.188	0.683	1.98	0.190	yes
29	0.393	2.21	2.09	0.170	0.652	2.00	0.190	yes
30	0.427	2.28	2.14	0.121	0.631	1.96	0.197	yes
31	0.480	2.32	2.19	0.131	0.749	1.92	0.233	no
33	0.587	2.34	2.21	0.209	0.826	1.90	0.250	no
45	0.405	2.17	2.05	0.202	0.747	2.09	0.188	yes
50	0.500	2.31	2.17	0.226	0.987	1.96	0.237	no
60	0.810	2.42	2.30	0.307	0.709	2.18	0.248	no
80	0.871	2.20	2.13	0.300	0.520	2.43	0.222	no
$V_{\rm ini} = 300\,{\rm km\,s^{-1}}$ $Z_\odot$								
15	0.199	1.88	1.81	0.158	0.732	2.40	0.153	yes
17	0.339	2.12	2.01	0.200	0.721	2.10	0.188	yes
19	0.408	2.30	2.16	0.212	0.707	1.99	0.180	yes
20	0.620	2.37	2.25	0.239	0.747	1.93	0.224	no
27	0.552	2.36	2.22	0.247	0.815	1.92	0.226	no
32	0.649	2.35	2.20	0.210	0.852	1.88	0.263	no
40	0.437	2.18	2.04	0.164	0.927	2.05	0.171	yes
50	0.484	2.32	2.18	0.219	0.847	1.98	0.195	yes
60	0.523	2.33	2.20	0.231	0.863	1.95	0.223	no
80	0.906	2.40	2.34	0.345	0.646	2.88	0.256	no
$V_{\rm ini} = 300\,{\rm km\,s^{-1}}$ $1/10\,Z_\odot$								
13	0.205	1.96	1.88	0.055	0.521	2.28	0.178	yes
15	0.171	1.84	1.77	0.142	0.713	2.43	0.139	yes
16	0.494	2.29	2.16	0.230	0.822	1.95	0.226	no
21	0.452	2.26	2.14	0.142	0.652	1.96	0.179	yes
26	0.291	2.12	2.02	0.131	0.651	2.10	0.169	yes
27	0.397	2.19	2.08	0.117	0.614	2.00	0.198	yes
28	0.537	2.26	2.15	0.237	0.728	1.96	0.224	no
35	0.593	2.30	2.16	0.184	0.784	1.90	0.227	no
60	0.942	2.46	2.36	0.321	0.665	2.93	0.257	no
$V_{\rm ini} = 300\,{\rm km\,s^{-1}}$ $1/50\,Z_\odot$								
15	0.205	1.88	1.81	0.151	0.723	2.40	0.151	yes
16	0.340	2.15	2.03	0.179	0.602	2.10	0.168	yes
19	0.316	2.08	1.98	0.188	0.617	2.15	0.172	yes
20	0.513	2.32	2.20	0.226	0.760	1.96	0.227	no
21	0.422	2.26	2.13	0.202	0.748	2.00	0.192	yes
26	0.366	2.19	2.07	0.156	0.592	2.01	0.177	yes
27	0.473	2.26	2.13	0.194	0.621	1.96	0.183	yes
28	0.590	2.38	2.24	0.172	0.713	1.90	0.229	no
30	0.656	2.36	2.22	0.236	0.773	1.92	0.252	no
35	0.664	2.33	2.22	0.249	0.823	2.06	0.222	no
40	0.803	2.62	2.49	0.249	0.857	4.49	0.251	no
$V_{\rm ini} = 600\,{\rm km\,s^{-1}}$ $Z_\odot$								
15	0.237	1.94	1.86	0.186	0.767	2.34	0.177	yes
21	0.470	1.96	2.05	0.194	0.663	2.15	0.191	yes
22	0.539	2.21	2.09	0.200	0.684	2.02	0.190	yes
23	0.574	2.29	2.16	0.238	0.742	1.97	0.198	yes
32	0.474	2.35	2.20	0.177	0.885	1.88	0.236	no
34	0.395	2.32	2.19	0.187	0.912	1.89	0.223	no
40	0.448	2.30	2.14	0.175	0.741	1.98	0.222	no
50	0.611	2.41	2.23	0.270	0.751	1.97	0.234	no
60	0.817	2.42	2.30	0.285	0.753	2.10	0.265	no
80	0.870	2.39	2.26	0.304	0.532	4.86	0.243	no
$V_{\rm ini} = 600\,{\rm km\,s^{-1}}$ $1/10\,Z_\odot$								
12	0.563	2.35	2.22	0.242	0.854	1.99	0.230	no
13	0.432	2.20	2.09	0.207	0.732	2.08	0.199	yes
15	0.145	1.75	1.69	0.145	0.692	2.75	0.148	yes
20	0.566	2.35	2.23	0.209	0.639	2.17	0.192	yes
21	0.625	2.29	2.19	0.156	0.608	2.43	0.234	no
22	0.656	2.31	2.20	0.162	0.682	2.36	0.237	no
28	0.519	2.33	2.18	0.151	0.809	1.99	0.183	yes
40	0.537	2.42	2.29	0.270	0.737	2.22	0.154	yes
45	0.745	2.49	2.37	0.243	0.703	2.12	0.243	no
55	0.885	2.46	2.35	0.253	0.672	2.53	0.263	no
$V_{\rm ini} = 600\,{\rm km\,s^{-1}}$ $1/50\,Z_\odot$								
15	0.511	2.36	2.23	0.219	0.738	2.14	0.191	yes
16	0.576	2.40	2.27	0.235	0.734	2.10	0.185	yes
19	0.640	2.46	2.31	0.205	0.673	2.42	0.242	no
22	0.440	2.16	2.04	0.157	0.744	2.08	0.194	yes
27	0.365	2.30	2.14	0.183	0.852	2.38	0.118	yes
28	0.413	2.33	2.18	0.192	1.240	2.29	0.168	yes
29	0.432	2.35	2.20	0.201	1.150	2.28	0.153	yes
31	0.589	2.46	2.33	0.249	0.907	2.40	0.192	yes
33	0.645	2.51	2.38	0.262	0.820	2.32	0.238	no
40	0.556	2.35	2.20	0.217	0.953	1.90	0.196	yes
50	0.802	2.48	2.36	0.309	0.770	2.35	0.258	no
60	0.874	2.49	2.37	0.302	0.891	3.99	0.283	no

Notes. ZAMS mass, $\xi_{2.5}$, $M_{\rm bary}$ and $M_{\rm grav}$ are the baryonic and gravitational masses (enclosed within the radius where the density equals $10^{12}\,{\rm g\,cm^{-3}}$, evaluated at the end of the simulations with $f_{\rm heat} = f_{\rm heat}^{\rm crit}$), shock formation time ($t_{\rm bounce}$), explosion time ($t_{\rm f}$), critical heating parameter at explosion ($f_{\rm heat}^{\rm crit}$), and corresponding ($\bar{\eta}_{\rm heat}^{\rm crit}$).

processes slow the core contraction down and lead to a reduced compactness. By examining the distribution of $\xi_{2.5}$ with respect to $M_{\rm ZAMS}$, we find that all model groups exhibit similar profiles. In the left and middle panels, the relation between $M_{\rm ZAMS}$ and $\xi_{2.5}$ is similar. In the right panel, the profile shifts toward lower-mass regions with decreasing metallicity. This shift arises because CHE occurs in the $1/10\,Z_\odot$ and $1/50\,Z_\odot$ model groups. A lower metallicity promotes more efficient CHE, which produces larger He cores and CO cores for the same $M_{\rm ZAMS}$ compared to higher-metallicity models.

Following Figure 5, we used our explodability criterion to determine the initial mass range for FSN. The left panel ($V_{\rm ini} = 0$) shows the explodability criterion of $\xi_{2.5} = 0.45$, and stars with initial masses between approximately 21 and 23 $M_\odot$, between 30 and 41 $M_\odot$, and above approximately 50 $M_\odot$ cannot undergo supernova explosions. These results are consistent with previous studies by Sukhbold et al. (2018), Ugliano et al. (2012), and Ivanov & Fernández (2021). For the middle panel ($V_{\rm ini} = 300\,{\rm km\,s^{-1}}$), based on $\xi_{2.5} = 0.48$, FSN forms in the initial mass ranges of approximately 20–22 $M_\odot$, 27–35 $M_\odot$, and above 40 $M_\odot$. For the right panel ($V_{\rm ini} = 600\,{\rm km\,s^{-1}}$), the results depend on the metallicity: At solar metallicity ($Z = Z_\odot$), the FSN initial mass range is ~14 $M_\odot$, 23–40 $M_\odot$, and above 50 $M_\odot$; for $1/10\,Z_\odot$, stars with $M_{\rm ZAMS}$ in the ranges of approx-

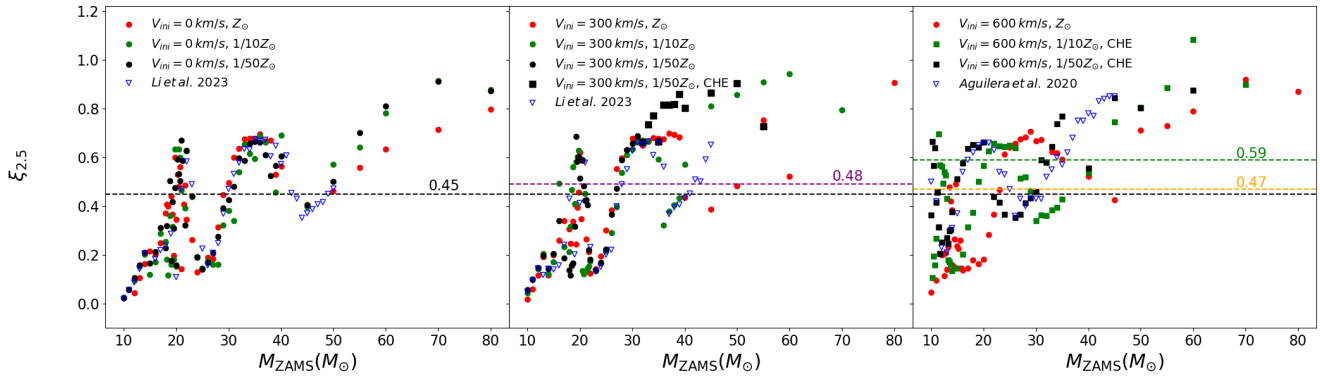

Fig. 5. $\xi_{2.5}$ vs. initial mass for models with varying initial rotational velocities $V_{\rm ini}$ and metallicities. The left, middle, and right panels correspond to models with $V_{\rm ini}$ = 0, 300 km s^{-1}, and 600 km s^{-1}, respectively. Metallicities of $Z_\odot$, 1/10 $Z_\odot$, and 1/50 $Z_\odot$are represented in red, green and black, respectively. The squares mark the occurrence of CHE. The left and middle blue triangles indicate model calculations from Li et al. (2023) (Z = 0.0017), and the right blue triangle denotes the rapidly rotating model from Aguilera-Dena et al. (2020) (1/50 $Z_\odot$). The dashed lines mark explosion criteria for $\xi_{2.5}$: the black line shows O'Connor & Ott (2011), and others from our results.

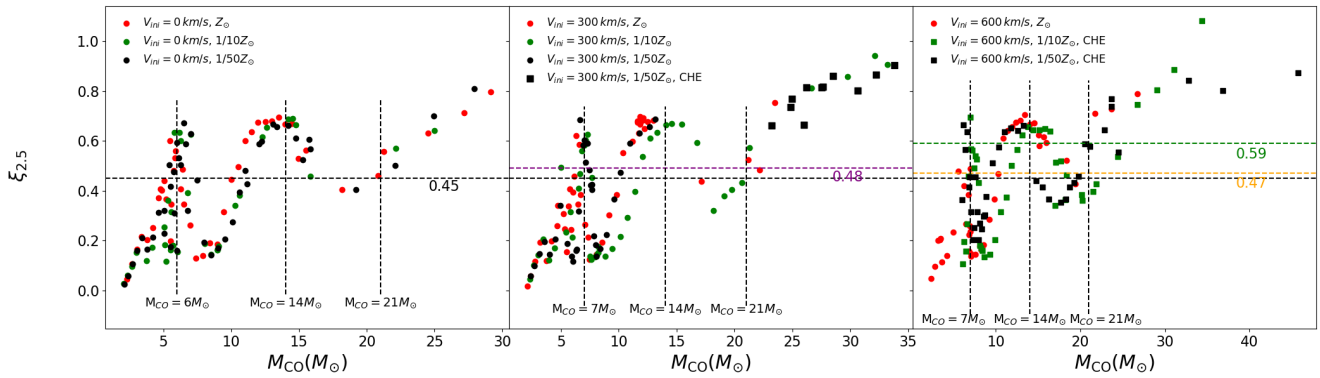

Fig. 6. $\xi_{2.5}$ vs. CO-core mass for models with varying initial rotational velocities $V_{\rm ini}$ and metallicities. The left, middle, and right panels correspond to models with $V_{\rm ini}$ = 0, 300 km s^{-1}, and 600 km s^{-1}, respectively. Metallicities of $Z_\odot$, 1/10 $Z_\odot$, and 1/50 $Z_\odot$ are shon in red, green, and black, respectively. The squares mark the occurrence of CHE.

imately ∼11 $M_\odot$, 21–26 $M_\odot$ and above 40 $M_\odot$ fail to undergo CCSN explosions; for 1/50 $Z_\odot$, stars with $M_{\rm ZAMS}$ in the ranges of approximately ∼11 $M_\odot$, 17–20 $M_\odot$ and above 32 $M_\odot$ fail to undergo CCSN explosions.

For models without CHE, the initial mass range for the occurrence of FSN differs slightly from the results obtained using the traditional criterion ($\xi_{2.5}$ = 0.45). In contrast, pre-supernova stars that have undergone CHE exhibit a reduced $M_{\rm ZAMS}$ range for forming FSN when the $\xi_{2.5}$ = 0.59 criterion is applied. Their cores maintain higher pre-supernova star angular velocities (see Fig. 3), and these systems (even when they fail to produce successful CCSN explosions) are therefore more likely to generate long gamma-ray bursts (lGRBs) (Woosley 1993; Yoon et al. 2006). This results in luminous transients that might not conform to the observational definition of FSN (Yoon et al. 2006). lGRBs are produced when the specific angular ($j_{\rm co}$) momentum at any location within the CO core exceeds that of the last stable orbit ($j_{\rm Kerr,LSO}$) (Bardeen et al. 1972). CHE progenitors undergoing core collapse leave bare CO cores and retain sufficient specific angular momentum during the black hole formation to facilitate lGRB production (Aguilera-Dena et al. 2018, 2020; Li et al. 2023).

Figure 6 shows the evolution of $\xi_{2.5}$ as a function of CO core mass at core collapse for different model groups. The trends in all model groups are comparable: Distinct compact regions of high $\xi_{2.5}$ appear at CO core masses of approximately 6–7 $M_\odot$, ∼14 $M_\odot$, and ≳21 $M_\odot$. These high-$\xi_{2.5}$ regions generally correspond to the domains that are favorable for failed supernova formation. Rotation and metallicity have very little effect on the overall distribution of $\xi_{2.5}$ with CO core mass. Models with CHE significantly narrow the CO core mass interval, however, which leads to failed supernovae (reducing the width of the peaks). It is noteworthy that the locations of the first two compact peaks observed in this study (at ∼7 $M_\odot$ and ∼14 $M_\odot$) are comparable to those reported by Temaj et al. (2024). These authors indicated that the location of the peak in the $\xi_{2.5}$ distribution versus CO core mass is affected by the convective-core overshooting value.

4. Conclusions

Using the MESA stellar evolution code, we simulated stars with initial rotational velocities of $V_{\rm ini}$ = 0, 300 km s^{-1}, and 600 km s^{-1} at three metallicities ($Z_\odot$, 1/10 $Z_\odot$, and 1/50 $Z_\odot$). We tracked their evolution from the ZAMS until iron-core collapse at 1000 km s^{-1}. Using the MESA models of iron-core collapse at 1000 km s^{-1}, we extracted key parameters (enclosed mass, temperature, density, radial velocity, electron fraction, and angular velocity) as input parameters for GR1D, and we subsequently simulated the CCSN phase with GR1D. We iteratively determined the critical value of $f_{\rm heat}$ such that it lay within 1% of

the threshold required for a successful explosion. The corresponding time-averaged heating efficiency at this critical $f_{\rm heat}$, denoted as $\bar{\eta}^{\rm crit}_{\rm heat}$, was then used to evaluate whether the progenitor can explode in multidimensional simulations. Finally, we established a correlation between the explosion outcomes and $\xi_{2.5}$, and we derived the critical compactness parameters $\xi_{2.5}$ for pre-supernova star explodability as follows: 0.45 for models with $V_{\rm ini} = 0$; 0.48 for the $V_{\rm ini} = 300\,{\rm km\,s^{-1}}$ group; 0.47 for $V_{\rm ini} = 600\,{\rm km\,s^{-1}}$ at $Z = Z_\odot$; and 0.59 for low metallicity ($Z = 1/10$ and $1/50\,Z_\odot$). These criteria enable a rapid assessment of pre-supernova stars explodability for EOS configurations resembling LS220. The upper limit of the pre-supernova star compactness for producing CCSNe is significantly higher in models where massive stars have undergone CHE compared to those without CHE. This discrepancy primarily arises because the centrifugal force generated by rotational motion in pre-supernova star more effectively facilitates explosions compared to nonrotating scenarios. Traditional criteria ($\xi_{2.5} = 0.45$) might not be suitable to evaluate the CHE progenitor explodability.

We established correlations between the explodability of stars in different model groups and their ZAMS masses. We determined the initial ZAMS mass ranges for an explosion formation in these groups. For models without CHE, the ZAMS mass ranges that lead to FSN vary less than the ranges obtained using the $\xi_{2.5} < 0.45$ explodability criterion. In contrast, model groups that underwent CHE showed a significantly increased initial ZAMS mass range for the occurrence of an explosion. They are more likely to produce lGRBs, which leads to a significantly reduced likelihood of FSN. Through our analysis of the compactness parameter $\xi_{2.5}$ distribution as a function of CO core mass, we found that for model groups with otherwise identical initial parameters, rotation and metallicity affect the distribution of compactness with CO-core mass only little.

Acknowledgements. We thank Evan O'Connor for helpful discussions and advice about using GR1D. This work received the support of the National Natural Science Foundation of China under grants 12373038, 12163005, U2031204 and 12288102; the Natural Science Foundation of Xinjiang No.2022TSYCLJ0006 and 2022D01D85.

References

Aguilera-Dena, D. R., Langer, N., Moriya, T. J., & Schootemeijer, A. 2018, ApJ, 858, 115
Aguilera-Dena, D. R., Langer, N., Antoniadis, J., & Müller, B. 2020, ApJ, 901, 114
Aguilera-Dena, D. R., Langer, N., Antoniadis, J., et al. 2022, A&A, 661, A60
Aguilera-Dena, D. R., Müller, B., Antoniadis, J., et al. 2023, A&A, 671, A134
Antoniadis, J., Aguilera-Dena, D. R., Vigna-Gómez, A., et al. 2022, A&A, 657, L6
Asplund, M., Grevesse, N., Sauval, A. J., & Scott, P. 2009, ARA&A, 47, 481
Bardeen, J. M., Press, W. H., & Teukolsky, S. A. 1972, ApJ, 178, 347
Bethe, H. A., & Wilson, J. R. 1985, ApJ, 295, 14
Bjorkman, J. E., & Cassinelli, J. P. 1993, ApJ, 409, 429
Boccioli, L., Mathews, G. J., & O'Connor, E. P. 2021, ApJ, 912, 29
Boccioli, L., Vartanyan, D., O'Connor, E. P., & Kasen, D. 2025, MNRAS, 540, 3885
Böhm-Vitense, E. 1958, Z. Astrophys., 46, 108
Brott, I., de Mink, S. E., Cantiello, M., et al. 2011, A&A, 530, A115
Bruenn, S. W., Lentz, E. J., Hix, W. R., et al. 2016, ApJ, 818, 123
Buras, R., Janka, H. T., Rampp, M., & Kifonidis, K. 2006a, A&A, 457, 281
Buras, R., Rampp, M., Janka, H. T., & Kifonidis, K. 2006b, A&A, 447, 1049
Burrows, A., Reddy, S., & Thompson, T. A. 2006, Nucl. Phys. A, 777, 356
Burrows, A., Radice, D., & Vartanyan, D. 2019, MNRAS, 485, 3153
Burrows, A., Radice, D., Vartanyan, D., et al. 2020, MNRAS, 491, 2715
Burrows, A., Vartanyan, D., & Wang, T. 2023, ApJ, 957, 68
Burrows, A., Wang, T., & Vartanyan, D. 2024, ApJ, 964, L16
Cardall, C. Y., Endeve, E., & Mezzacappa, A. 2013, Phys. Rev. D, 87, 103004
Chan, C., Müller, B., Heger, A., Pakmor, R., & Springel, V. 2018, ApJ, 852, L19
Colgate, S. A., & White, R. H. 1966, ApJ, 143, 626
Couch, S. M., Warren, M. L., & O'Connor, E. P. 2020, ApJ, 890, 127
Diehl, R., Lugaro, M., Heger, A., et al. 2021, PASA, 38, e062
Ertl, T., Janka, H. T., Woosley, S. E., Sukhbold, T., & Ugliano, M. 2016, ApJ, 818, 124
Farrell, E. J., Groh, J. H., Meynet, G., & Eldridge, J. J. 2020, MNRAS, 494, L53
Fischer, T., Whitehouse, S. C., Mezzacappa, A., Thielemann, F. K., & Liebendörfer, M. 2009, A&A, 499, 1
Fischer, T., Bastian, N.-U., Blaschke, D., et al. 2017, PASA, 34, e067
Fryer, C. L., & Warren, M. S. 2002, ApJ, 574, L65
Gogilashvili, M., Murphy, J. W., & O'Connor, E. P. 2023, MNRAS, 524, 4109
Halevi, G., Wu, B., Mösta, P., et al. 2023, ApJ, 944, L38
Hamann, W. R., Koesterke, L., & Wessolowski, U. 1995, A&A, 299, 151
Heger, A., & Langer, N. 2000, ApJ, 544, 1016
Heger, A., Langer, N., & Woosley, S. E. 2000, ApJ, 528, 368
Heger, A., Müller, B., & Mandel, I. 2023, ArXiv e-prints [arXiv:2304.09350]
Henneco, J., Schneider, F. R. N., & Laplace, E. 2024, A&A, 682, A169
Herant, M., Benz, W., Hix, W. R., Fryer, C. L., & Colgate, S. A. 1994, ApJ, 435, 339
Horiuchi, S., Beacom, J. F., Kochanek, C. S., et al. 2011, ApJ, 738, 154
Horowitz, C. J. 2002, Phys. Rev. D, 65, 043001
Ivanov, M., & Fernández, R. 2021, ApJ, 911, 6
Janka, H. T. 2001, A&A, 368, 527
Janka, H.-T. 2012, Annu. Rev. Nucl. Part. Sci., 62, 407
Janka, H.-T. 2017, in Handbook of Supernovae, eds. A. W. Alsabti, & P. Murdin, 1095
Janka, H. T. 2025, ArXiv e-prints [arXiv:2502.14836]
Janka, H. T., & Mueller, E. 1996, A&A, 306, 167
Janka, H.-T., Melson, T., & Summa, A. 2016, Annu. Rev. Nucl. Part. Sci., 66, 341
Kobulnicky, H. A., & Fryer, C. L. 2007, ApJ, 670, 747
Kuroda, T., Kotake, K., Takiwaki, T., & Thielemann, F.-K. 2018, MNRAS, 477, L80
Langer, N. 1992, A&A, 265, L17
Langer, N. 1998, A&A, 329, 551
Laplace, E., Justham, S., Renzo, M., et al. 2021, A&A, 656, A58
Laplace, E., Schneider, F. R. N., & Podsiadlowski, P. 2025, A&A, 695, A71
Lattimer, J. M., & Swesty, D. F. 1991, Nucl. Phys. A, 535, 331
Lentz, E. J., Bruenn, S. W., Hix, W. R., et al. 2015, ApJ, 807, L31
Li, W., Leaman, J., Chornock, R., et al. 2011, MNRAS, 412, 1441
Li, L., Zhu, C., Guo, S., Liu, H., & Lü, G. 2023, ApJ, 952, 79
Li, Z., Lu, X., Lü, G., et al. 2025, ApJ, 979, L37
Liebendörfer, M., Rampp, M., Janka, H. T., & Mezzacappa, A. 2005, ApJ, 620, 840
Limongi, M., & Chieffi, A. 2018, ApJS, 237, 13
Mabanta, Q. A., & Murphy, J. W. 2018, ApJ, 856, 22
Maeder, A., & Meynet, G. 1987, A&A, 182, 243
Maltsev, K., Schneider, F. R. N., Mandel, I., et al. 2025, A&A, 700, A20
Marchant, P., Langer, N., Podsiadlowski, P., Tauris, T. M., & Moriya, T. J. 2016, A&A, 588, A50
Miller, D. S., Wilson, J. R., & Mayle, R. W. 1993, ApJ, 415, 278
Moe, M., & Di Stefano, R. 2017, ApJS, 230, 15
Müller, B. 2015, MNRAS, 453, 287
Müller, B., Heger, A., Liptai, D., & Cameron, J. B. 2016, MNRAS, 460, 742
Müller, B., Melson, T., Heger, A., & Janka, H.-T. 2017, MNRAS, 472, 491
Müller, B., Tauris, T. M., Heger, A., et al. 2019, MNRAS, 484, 3307
Murphy, J. W., & Burrows, A. 2008, ApJ, 688, 1159
Obergaulinger, M., & Aloy, M. Á. 2020, MNRAS, 492, 4613
O'Connor, E. 2015, ApJS, 219, 24
O'Connor, E., & Ott, C. D. 2010, CQG, 27, 114103
O'Connor, E., & Ott, C. D. 2011, ApJ, 730, 70
O'Connor, E., Bollig, R., Burrows, A., et al. 2018, J. Phys. G Nucl. Phys., 45, 104001
Ott, C. D., Burrows, A., Dessart, L., & Livne, E. 2008, ApJ, 685, 1069
Paxton, B., Bildsten, L., Dotter, A., et al. 2011, ApJS, 192, 3
Paxton, B., Cantiello, M., Arras, P., et al. 2013, ApJS, 208, 4
Paxton, B., Marchant, P., Schwab, J., et al. 2015, ApJS, 220, 15
Paxton, B., Schwab, J., Bauer, E. B., et al. 2018, ApJS, 234, 34
Paxton, B., Smolec, R., Schwab, J., et al. 2019, ApJS, 243, 10
Pejcha, O., & Thompson, T. A. 2015, ApJ, 801, 90
Radice, D., Burrows, A., Vartanyan, D., Skinner, M. A., & Dolence, J. C. 2017, ApJ, 850, 43
Saio, H., Nomoto, K., & Kato, M. 1988, Nature, 334, 508
Sana, H., de Mink, S. E., de Koter, A., et al. 2012, Science, 337, 444
Sana, H., de Koter, A., de Mink, S. E., et al. 2013, A&A, 550, A107
Sana, H., Le Bouquin, J. B., Lacour, S., et al. 2014, ApJS, 215, 15
Scheck, L., Kifonidis, K., Janka, H. T., & Müller, E. 2006, A&A, 457, 963
Schneider, F. R. N., Podsiadlowski, P., & Müller, B. 2021, A&A, 645, A5

Schneider, F. R. N., Podsiadlowski, P., & Laplace, E. 2023, ApJ, 950, L9
Schneider, F. R. N., Podsiadlowski, P., & Laplace, E. 2024, A&A, 686, A45
Shibata, M., Kiuchi, K., Sekiguchi, Y., & Suwa, Y. 2011, Prog. Theor. Phys., 125, 1255
Smartt, S. J. 2015, PASA, 32, e016
Stegmann, J., Antonini, F., & Moe, M. 2022, MNRAS, 516, 1406
Sukhbold, T., & Woosley, S. E. 2014, ApJ, 783, 10
Sukhbold, T., Ertl, T., Woosley, S. E., Brown, J. M., & Janka, H. T. 2016, ApJ, 821, 38
Sukhbold, T., Woosley, S. E., & Heger, A. 2018, ApJ, 860, 93
Summa, A., Janka, H.-T., Melson, T., & Marek, A. 2018, ApJ, 852, 28
Takahashi, K., Takiwaki, T., & Yoshida, T. 2023, ApJ, 945, 19
Takiwaki, T., Kotake, K., & Suwa, Y. 2016, MNRAS, 461, L112
Temaj, D., Schneider, F. R. N., Laplace, E., Wei, D., & Podsiadlowski, P. 2024, A&A, 682, A123
Timmes, F. X., Woosley, S. E., & Weaver, T. A. 1996, ApJ, 457, 834
Ugliano, M., Janka, H.-T., Marek, A., & Arcones, A. 2012, ApJ, 757, 69
Vartanyan, D., & Burrows, A. 2023, MNRAS, 526, 5900
Vartanyan, D., Laplace, E., Renzo, M., et al. 2021, ApJ, 916, L5
Vink, J. S., de Koter, A., & Lamers, H. J. G. L. M. 2001, A&A, 369, 574
Wang, T., Vartanyan, D., Burrows, A., & Coleman, M. S. B. 2022, MNRAS, 517, 543
Woosley, S. E. 1993, ApJ, 405, 273
Woosley, S. E., & Weaver, T. A. 1995, ApJS, 101, 181
Woosley, S. E., Sukhbold, T., & Janka, H. T. 2020, ApJ, 896, 56
Yoon, S. C., Langer, N., & Norman, C. 2006, A&A, 460, 199
Yoshida, T., Takiwaki, T., Aguilera-Dena, D. R., et al. 2021, MNRAS, 506, L20

Appendix A: Grid simulations at higher resolution

We set a high-resolution grid comprising 1200 radial zones. Within the inner 20 km, 200 radial zones are configured at a fine spacing of 100 m. Beyond 20 km, the grid extends logarithmically to an outer boundary where the density reaches 2000 g cm^{-3}.

Figure A.1 shows the shock radius evolution with time $t_{\rm bounce}$ for different $f_{\rm heat}$ values. (The four pre-supernova star models simulated in here are identical to those presented in Figures 2 and 3 of the main text). Comparisons of simulations at different grid resolutions indicate that at low $f_{\rm heat}$ values, results from both grid resolutions are nearly identical. As $f_{\rm heat}$ increases, simulations remain consistent until the early shock stagnation phase; beyond this point, however, the finer grid demonstrates a higher likelihood of shock revival and explosion. Simulations of the identical initial setup performed at varying grid resolutions yield deviations in $f_{\rm heat}^{\rm crit}$ that average less than 3%.

Figure A.2 depicts the temporal evolution of $L_{\bar{\nu}_e,\nu_e}$ at the gain radius and $\dot{Q}_\nu$ in the critical model across different grid resolutions. We calculate the critical heating efficiency parameters $\bar{\eta}_{\rm heat}^{\rm crit}$ for the 1200 grid configuration, with the upper panel (left to right) corresponding to 0.109 and 0.129, and the lower panel (left to right) to 0.246 and 0.253.

The results indicate a mean relative deviation of $\sim$ 3% in $\bar{\eta}_{\rm heat}^{\rm crit}$ between grid configurations. Given that simulations with high-resolution grids require over five times the computational resources of their low-resolution counterparts, we employed the low-resolution setup (600 total cells) for all models.

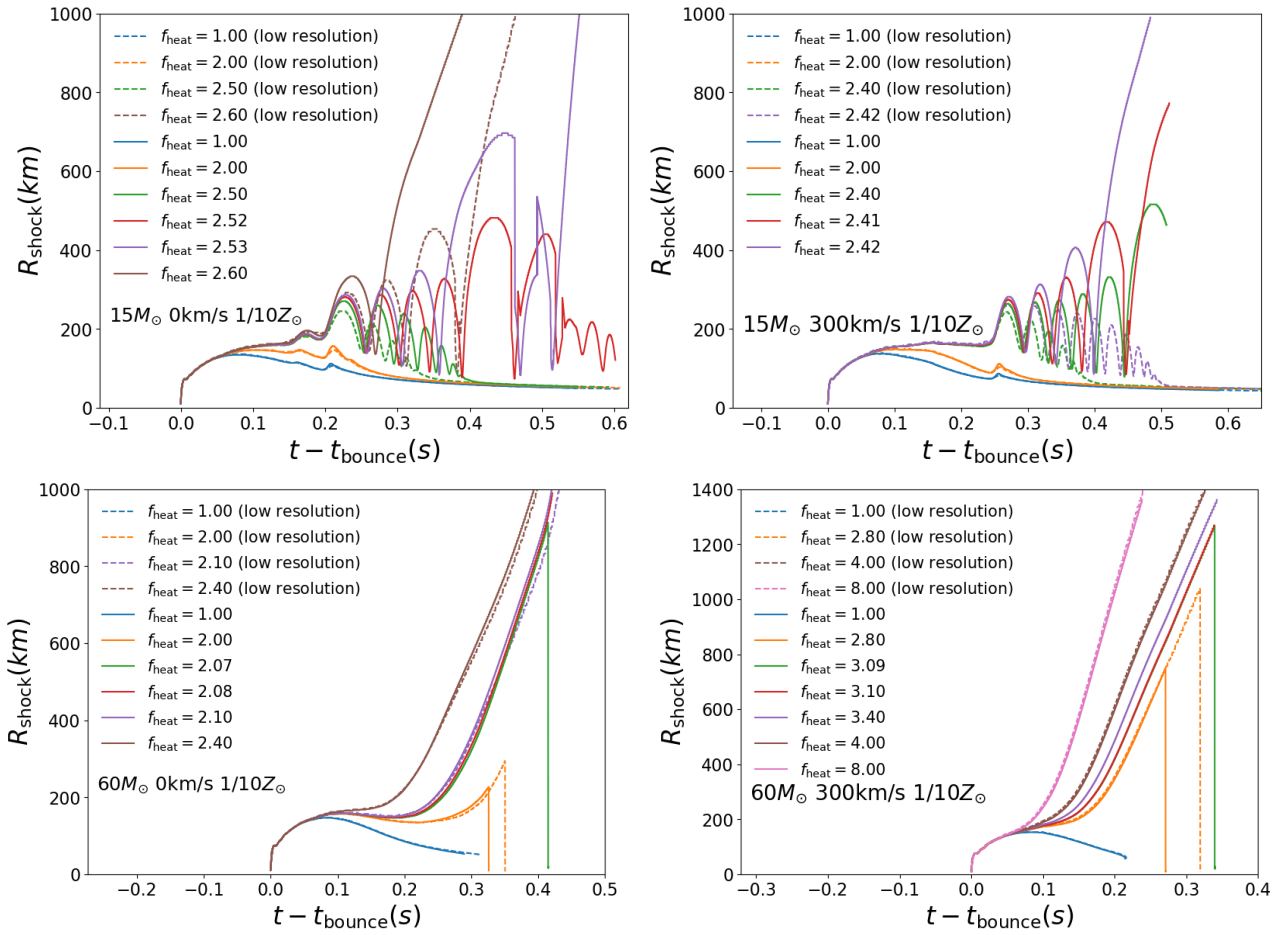

Fig. A.1. Shock wave radius evolution vs. explosion time $t_{\rm bounce}$ for different $f_{\rm heat}$ values. The simulations started with an iron core-collapse velocity of 1000 km s^{-1}, where $t = 0$ corresponds to shock wave formation. Dashed curves depict simulations employing coarse numerical grids, while solid lines correspond to higher-resolution implementations. The top and bottom panels show 15 M$_\odot$ and 60 M$_\odot$ ZAMS masses respectively, with initial velocities $V_{\rm ini} = 0$ (left panels) and 300 km s^{-1} (right panels). All models have a metallicity of 1/10 Z$_\odot$.

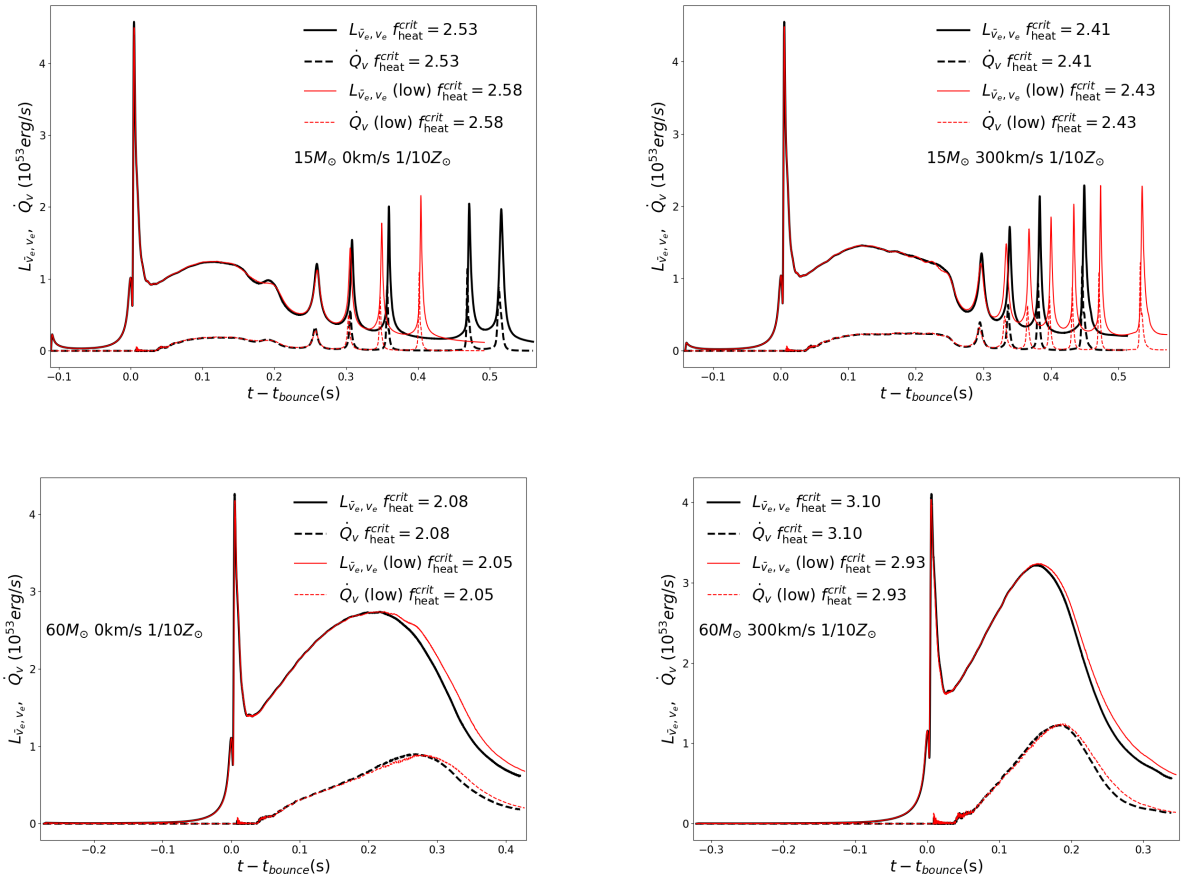

Fig. A.2. For $f_{\rm heat} = f^{\rm crit}_{\rm heat}$, we show the evolution of the electron neutrino and antineutrino luminosities $L_{\bar{\nu}_e,\nu_e}$ (solid lines) at the gain radius and net neutrino energy deposition rate in the gain layer $\dot{Q}_\nu$ ($\int_{\rm gain} \dot{q}^+_\nu \, dV$, dashed lines) vs. time $t_{\rm bounce}$. The simulations started with an iron core-collapse velocity of 1000 km s^{-1}, where $t = 0$ corresponds to the shock wave formation. The red lines depict simulations employing coarse numerical grids, while black curves correspond to higher-resolution implementations. The top and bottom panels show 15 $M_\odot$ and 60 $M_\odot$ ZAMS masses respectively, with initial velocities $V_{\rm ini} = 0$ (left panels) and 300 km s^{-1} (right panels). All models have a metallicity of $1/10$ $Z_\odot$.